

Article

Laboratory Studies on Nearshore Density-Driven Exchange Flow over a Partly Vegetated Slope

Zhenghua Gu ¹, Hao-Che Ho ², Zijing Wang ³ and Ying-Tien Lin ^{3,*} 

¹ Institute of Hydrology and Water Resources, College of Civil Engineering and Architecture, Zhejiang University, Hangzhou 310058, China; wise@zju.edu.cn

² Department of Civil Engineering, National Taiwan University, Taipei 10617, Taiwan; haocheho@ntu.edu.tw

³ Institute of Port, Coastal and Offshore Engineering, Ocean College, Zhejiang University, Hangzhou 310058, China; 3150100587@zju.edu.cn

* Correspondence: kevinlin@zju.edu.cn; Tel.: +86-157-001-51516

Received: 15 June 2018; Accepted: 9 August 2018; Published: 11 August 2018



Abstract: Density-driven exchange flows, which are important to the transport of nutrients, pollutants and chemical substances without external forcing, were studied through laboratory lock-exchange experiments. Rigid and emergent cylinders were placed in one of two reservoirs in a partitioned wedge-shaped tank to simulate a partly vegetated slope. The experimental results found that cylinders placed on only one side of the tank lead to different current speeds in the current head and tail that subsequently create various flow patterns and significantly affect the downslope current motions. By fitting with the experimental data, some unknown coefficients can be obtained in the theoretical formulae that are able to predict the intrusion length and exchange flowrate in real field systems. Compared to the flat bed cases, the total exchange discharge over a steep slope decreases by up to 4% for vegetation distributed in shallow water and increases by 14% for vegetation distributed in deeper regions. These results suggest that bed slope and vegetation distribution are crucial to the density-driven exchange flows in the flushing of nearshore regions.

Keywords: convective exchange flows; rigid and emergent vegetation; sloping bed

1. Introduction

In aquatic environments, convective exchange flows play an important role in the transport of nutrients, pollutants and chemical substances between the littoral and pelagic regions of lakes or reservoirs under weak wind conditions and in the absence of other sources of momentum (e.g., river flows) [1–3]. The convective exchange flows are mainly driven by a density difference in the horizontal direction, which can be caused by nearshore topographic changes [4], vegetation shading [5], or turbid patches in the water [6]. Convective circulation induced by topographic effects is most commonly found under typical field conditions. The spatially uniform solar radiation during the day leads to warmer water in the shallows than in the adjacent deeper regions, and this developing contrast in temperature between shallow and deep waters produces variations in water density that generate convective water exchange [7]. During the night, the condition is reversed, i.e., shallow regions cool more rapidly than deeper regions, which can drive convective circulation in the opposite direction to that during the day [7]. Thus, the diurnal heating and cooling processes can cause alternating convective circulation, enhancing the exchange of nutrients and chemical substances, and reducing the flushing time between the nearshore and the main parts of water bodies [8]. This process has been studied through field observations [4,9], laboratory experiments [10,11] and numerical modeling [7,12,13]. For example, Monismith et al. [4] and Adam and Wells [9] observed a significant time lag for circulation induced by alternating diurnal heating and cooling forcing in the nearshore. Later, Farrow and

Patterson [7] used a simplified diurnal model to confirm analytically that the time lag can be up to 12 h. The dominant physical mechanisms driving exchange circulation at different water depths have also been discussed. Lei and Patterson [14] revealed that deep-water thermal instability is crucial for disrupting the residual flow and reversing the circulation during diurnal cycles. These studies provide a solid understanding of the transient and constant components of convective exchange flow resulting from nearshore topography.

Shading from emergent or floating vegetation can also affect water temperature, leading to differential heating and cooling between vegetated regions and open water [15]. Dense stands of vegetation can intercept more incident sunlight, so water temperature in vegetated areas is cooler than that of the adjacent open water during daytime [16]. Similarly, during nighttime, emergent vegetation can reduce radiation losses so that the open water is cooler than that in the vegetated region [17]. Previous research has indicated that the differences in temperature between vegetated regions and open water can be sufficiently large (maximum $\Delta T \approx 2 - 4$ °C) to produce obvious temperature gradients and near-surface flow from illuminated to shaded areas [16–18]. Lövstedt and Bengtsson [16] observed that the surface flow exchange between emergent vegetation (reeds) and open water could be as much as 1.5 cm/s in the littoral zones of a lake. Coates and Ferris [19] revealed that shading from floating plants could generate exchange flows that are displaced downward due to the roots. In contrast, the inherently resistant forces of rooted vegetation significantly reduce current speed and volumetric exchange flowrates while increasing flushing time [8,20]. Tanino et al. [5], Zhang and Nepf [8] and Zhang and Nepf [20] modeled vegetative drag using a very common quadratic law. Zhang and Nepf [5] investigated the combined effects of shading and drag from emergent and rooted vegetation on thermally driven flow over a flat bed and reported that the exchange flow was inertia-dominated in the initial stage and rapidly transitioned to being drag-dominated. Tsakiri et al. [21] further concluded that when the vegetation density exceeded 15%, the exchange flow became drag-dominated from the beginning of the process. However, littoral aquatic vegetation commonly grows over a sloping bed rather than a flat bed, and vegetation is non-uniformly distributed from onshore to offshore due to variations in the supply of light and nutrients at different water depths [22]. Therefore, the combined effects of topography and vegetation shading on density-driven flow cannot be ignored.

Based on a simplified diurnal heating and cooling model, Lin and Wu [23] theoretically revealed the induced circulation patterns within rigid and emergent vegetation over a slope. It was found that vegetative drag plays an important role in reducing the magnitude of circulation and the time lag between the reversal of diurnal forcing and circulation, especially in deep waters. They also showed that the distribution of the vegetation could significantly alter circulation patterns and exchange flowrates. In addition, if the water column is thermally stratified, i.e., temperature varies with the vertical position in the water column, flow patterns become more complicated within non-uniformly distributed vegetation [24]. Recently, Ho and Lin [25] conducted laboratory lock-exchange experiments over a slope within uniformly and fully emergent and rigid vegetation. Assuming the distribution of hydrostatic pressure within gravity currents, several theoretical formulae were developed, which are provided in Section 2.

They revealed that the current head would accelerate over the downslope course if the cylinder density was less than 2%. However, in real field conditions with a non-uniform or partly vegetated slope, vegetation distributed on one side and open water on the other side of the slope are frequently found and the dynamic features of density currents could be different under such conditions. Additionally, exchange flowrates, which are the quantities of greatest interest in the transport of nutrients, pollutants, and chemical substances, were not the primary focus in their study.

In this study, we aim to address the following research questions: whether a sloping bed and vegetation distribution can significantly alter flow patterns, and how much of the flow intrusion length and total exchange discharge can be influenced. To answer these questions, brine-water lock-exchange experiments, commonly used to study thermally driven exchange flow [5,8], were carried out. This study is an extension of work by Ho and Lin [25] that focuses solely on convective exchange

flows within a uniformly and fully distributed canopy. Rigid and emergent cylinders were used to mimic aquatic canopies, such as reeds, with various experimental configurations including model canopies on both sides of the tank or a model canopy on either side. In contrast to the work of Ho and Lin [25], this new configuration (a model canopy on one side and open water on the other) can better simulate real field conditions, where an exchange flow is more likely to be produced by vegetation shading. As stated by Zhang and Nepf [20], although the experiment is a simplification of the field situation in which the difference in density varies over the course of the diurnal heating process, the setup and transient time scale for the exchange flow is short compared with the time scale of the diurnal temperature variations. Thus, the results from these simplified experiments are reasonable and applicable for evaluating the scales of the speeds and exchange flow rates of the current. The paper is arranged as follows. In Section 2, we describe the theoretical background for predicting the speed of the current as well as the total exchange volume discharge between open and vegetated regions. The experimental methods including setup, image acquisition, and data analysis are described in Section 3, and the experimental results are presented in Section 4 and discussed in Section 5. The conclusions are drawn in Section 6.

2. Mathematical Formulation

The theoretical formulae derived in Ho and Lin [25] are briefly described. Without a model canopy, the frontal velocities u_{lower} and u_{upper} in the lower and upper layers are given by (see Figure 1 in [25]):

$$u_{lower} = \sqrt{g'(C_1 L_{lower} S_0 + C_2 H_L)}, \quad (1)$$

$$u_{upper} = \sqrt{g'(-C_3 L_{lower} S_0 + C_4 H_L)}, \quad (2)$$

where g' is the reduced gravity; S_0 is the tank slope; L_{lower} and L_{upper} are the current lengths in the lower and upper layers; and H_L is the depth at the lock. C_1 , C_2 , C_3 and C_4 are coefficients that reflect the mixing and entrainment of the gravity current head with the ambient fluids and should be different for u_{lower} and u_{upper} . Over a flat bottom, i.e., $S_0 = 0$, Equations (1) and (2) are equivalent to the classic formula of current speed, $u = \sqrt{C_2 g' H_L}$ derived by Benjamin [26], in which $C_2 = C_4 = \frac{1}{4}$. Over a slope where vegetation is uniformly distributed, the drag-dominated frontal velocities $u_{v,lower}$ and $u_{v,upper}$ in the lower and upper layers are as follows [25]:

$$u_{v,lower} = \sqrt{-\frac{2n}{C_D a} \left(g' \frac{\partial \eta}{\partial x} \Big|_{\eta=0} - C_1 g' S_0 \right)}, \quad (3)$$

$$u_{v,upper} = \sqrt{-\frac{2n}{C_D a} \left(g' \frac{\partial \eta}{\partial x} \Big|_{\eta=0} + C_3 g' S_0 \right)}, \quad (4)$$

where C_D is the drag coefficient; a is the frontal area of the vegetation stems per unit volume; and η is the interfacial profile of the current. If the interface of the gravity currents within a model canopy also forms an inclined straight line as over a flat bed, the horizontal interface gradient $\partial \eta(x, t) / \partial x$ can be represented as:

$$\frac{\partial \eta(x, t)}{\partial x} = -s \frac{H_L + L_{lower} S_0}{L_{upper} + L_{lower}} = -s \frac{H_L - h_d}{L_{lower}}, \quad (5)$$

where s is a scale constant which accounts for the non-linearity of $\partial \eta(x, t) / \partial x$ and $s = 0.6$ as proposed by Tanino et al. [8], and h_d is the thickness of the density currents at the lock ($x = 0$) (Figure 1).

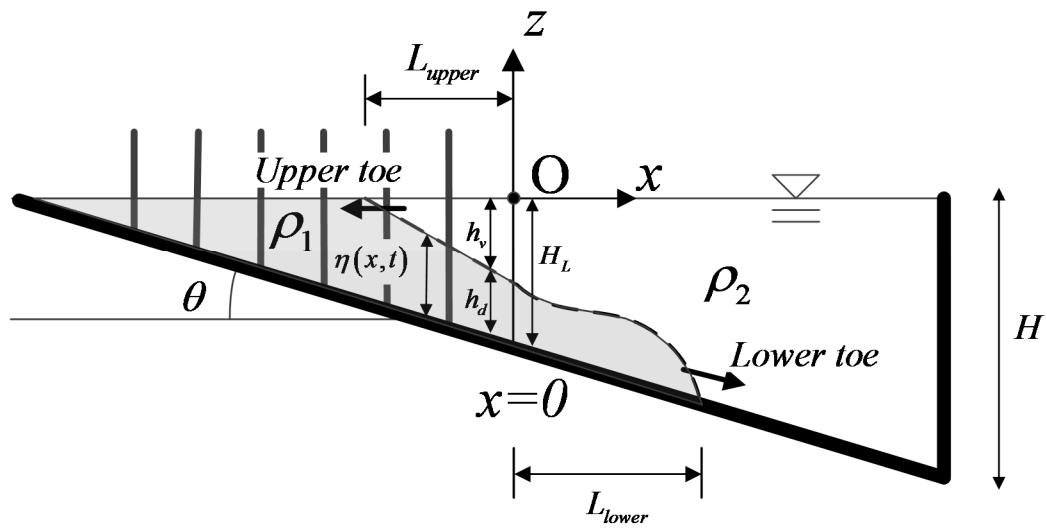


Figure 1. Schematic of a lock-exchange experiment with a model canopy distributed in a shallow region. The maximum water depth is H , and the lock is positioned at $x = 0$, i.e., the center of the tank, with a water depth of $H_L (= \frac{1}{2}H)$. $\eta(x, t)$ is the interface between two different fluid densities, and L_{lower} and L_{upper} are the horizontal distances of the interfaces from the lock in the lower and upper layers, respectively. ρ_1 and ρ_2 are the densities of heavier and lighter fluids, respectively.

If the current motion is over a flat bottom, i.e., $S_0 = 0$, u_v becomes the result derived by Tanino et al. [8]. In this study, the formula related to gravity current motions within uniform vegetation [25] is further extended to estimate the intrusion length and exchange flow discharge within partly vegetated conditions.

Herein, we consider that vegetation only occupies one side of the experimental tank and the dense fluid is initially in shallow regions, as shown in Figure 1. The motions of the flow after gate removal are influenced by vegetative drag after a short inertial period, and thus it can be expected that Equations (3) and (4), derived in a vegetative drag-dominated regime, will still be valid on the vegetated side of the tank. From Equations (3) and (4), the intrusion length L_v of the currents within the canopy can be expressed as:

$$u_v = \frac{dL_v}{dt} = \sqrt{-\frac{2n}{C_{Da}} \left(g' \frac{\partial \eta}{\partial x} \Big|_{\eta=0} \pm C_1(\text{or } C_3) g' S_0 \right)}. \tag{6}$$

Since h_d and L_{lower} in Equation (5) are unknown functions and vary with time, it is difficult to obtain the analytic form for L_v . Instead, L_v can be written as:

$$L_v = \sqrt{\frac{2ng'H_L}{C_{Da}}} f_1(t, S_0). \tag{7}$$

The total exchange volume per unit width, V , that has entered the vegetation can be estimated geometrically (if the interfacial profile of currents follows an inclined straight line, see Figure 1) as below:

$$V = \frac{1}{2} L_v h_v = \sqrt{\frac{2ng'H_L}{C_{Da}}} f_2(t, S_0), \tag{8}$$

where $h_v (= H_L - h_d)$ is the thickness of the light fluid entering the vegetation measured at $x = 0$. Consequently, the volumetric discharge rate per unit width ($= \frac{dV}{dt}$) should also be a function of time t and tank slope S_0 . When the gravity currents flow over a flat bottom with the model canopy

distributed on only one side and h_d is assumed constant, L_v , V and q can be analytically expressed as [20]:

$$L_v = \left[\frac{3}{2} \sqrt{\frac{ngtsH}{C_D a}} (t - t_0) \right]^{2/3}, \quad (9)$$

$$V = \frac{1}{2} \alpha H \left[\frac{3}{2} \sqrt{\frac{ngtsH}{C_D a}} (t - t_0) \right]^{2/3}, \quad (10)$$

$$q = \frac{1}{3} \alpha H \left[\frac{3}{2} \sqrt{\frac{ngtsH}{C_D a}} \right]^{2/3} (t - t_0)^{-1/3}, \quad (11)$$

where $\alpha = \frac{h_v}{H}$ is the ratio of the thickness of the gravity current to water depth at $x = 0$.

The vegetative drag, C_D , is crucial to the estimation of quantities such as L_v , V and q . For a smooth and isolated circular cylinder, C_D can be represented as:

$$C_D \approx 1 + 10Re_{cy}^{-2/3}, \quad (12)$$

in the range of $1 < Re_{cy} < 10^5$ [27], where $Re_{cy} \left(= \frac{ud}{\nu} \right)$ (u is the flow velocity, d is the diameter of the cylinder, and ν is the kinematic viscosity of fluid) is the cylinder Reynolds number. For an array of cylinders, Jamali et al. [28] suggested that the coefficient 10 in Equation (12) be replaced by 50 based upon the best match between a numerical simulation and experimental data. Thus, the expression is adopted for C_D in this study:

$$C_D \approx 1 + 50Re_{cy}^{-2/3} \quad (13)$$

3. Experimental Methods

The experimental methods are similar to those used in Ho and Lin [25], so we keep the repetitive descriptions to a minimum in this section. The wedge-shaped tanks used in the experiments had a rectangular, 0.25 m-wide by 0.8 m-long, cross-section and three different bottom slopes, S_0 , of 0.075 ($\sim 4.3^\circ$), 0.125 ($\sim 7.1^\circ$), and 0.25 ($\sim 14.0^\circ$), with transparent Plexiglas sidewalls. All tanks were separated into two regions of equal length by a removable, 5-mm thick partition, and rigid wooden sticks (0.3-cm diameter, d) and chopsticks (0.5-cm diameter, d) were used to model rigid and emergent aquatic vegetation such as reeds that typically have a diameter, d , between 0.1 and 1 cm [29]. The thickness of the partition (~ 5 mm) is very small compared with the length of the tank so that the influence of this thickness can be neglected, as done in much of the previous research [30]. Polyvinylchloride (PVC) sheets perforated with uniformly distributed holes (flow-aligned patterns) were placed on top of the tank to guide the placement of the model vegetation; the wood sticks or chopsticks were pushed through the holes to reach the tank bottom (see Figure 2). A 0.5-cm gap was left between the perforated sheet and the water surface to prevent friction from the upper PVC sheets. Different experimental configurations were considered in this study including a model canopy distributed in either shallow or deeper water with open water on the other side (see Figure 2). For comparison, some configurations included model canopies on both sides of the tank or no model canopy on either side.

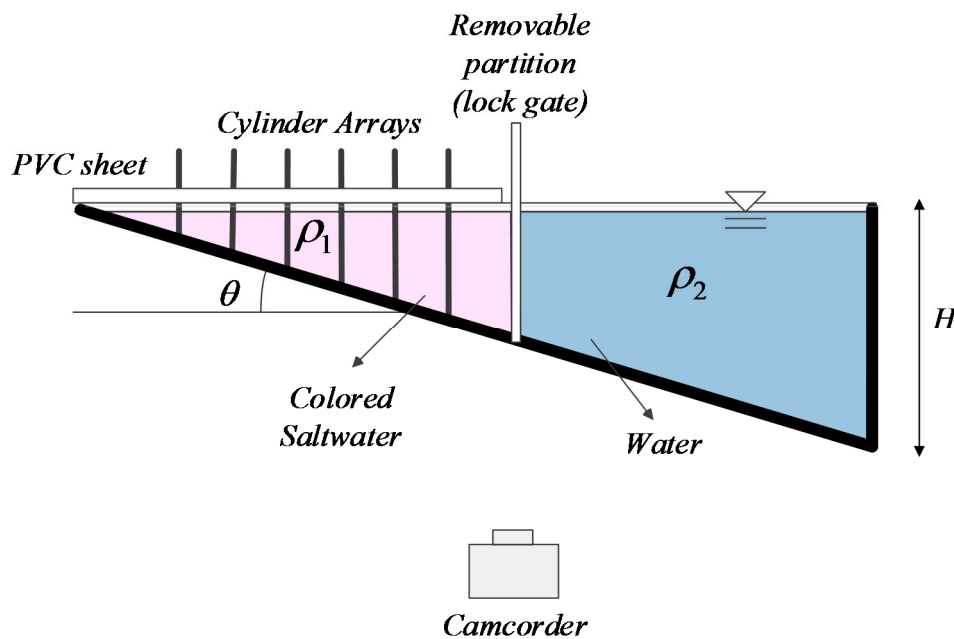


Figure 2. Set-up of a lock-exchange experiment with a model canopy distributed in a shallow region.

The density of the model canopy, ϕ , ranged between 0 and 0.069, producing a dimensionless array density of $ad = 0$ to 0.088, which is comparable to the ad values between 0.01 to 0.1 for natural canopies [31]. The shallow region was filled with well-mixed saltwater of density ρ_1 , and the deep regions were filled with freshwater of density ρ_2 (see Figure 2). For flow visualization, the saltwater was dyed with a dark-colored food dye, and images of the flow patterns were captured with a Canon VIXIA HF R400 camcorder (1920 × 1080-pixel resolution at 30 fps). The camcorder were placed 2.5 m away and normal to the sidewall of the tanks. By rapidly lifting up the partition, gravity currents were produced down the slope. After the data was collected, a binary image thresholding technique was applied to delineate the current boundary [20,32]. The colored images were firstly converted to binary pictures by using the commercial software Matlab. The threshold was manually chosen such that the binary images (the gravity current body is white and the rest is black) gave the best agreement with the visible saline-ambient interface. By detecting the edge of the white region, the contour of areas occupied by the colored-saline, i.e., the gravity current body, can be clearly identified and delineated, which can later be used to obtain current thickness (the vertical distance from the upper boundary of the gravity current to the tank bottom), foremost locations and area of the colored regions, etc. Assuming the gravity current motion is two-dimensional, the colored areas multiplied by the tank width can represent the volume of exchange density flows. Then, the temporal volumetric discharge can be estimated through time-series experimental images.

The measurement uncertainties mainly from the pixel resolution, image thresholding and obstruction of modeled vegetation are less than 3% of measurements in the absence of modelled vegetation, but up to 5–10% of measurements in dense vegetation population ($\phi = 0.069$) due to the obscure current head within vegetation. Since the current velocities in the upper and lower toes are different, the entrainment and mixing between the current and ambient fluids are also varied, i.e., the areas occupied by the gravity current, namely, the colored areas in the downslope and upslope sides may not be equal. The colored areas in the upslope side are sometimes fuzzy due to the reflection from the water surface; hence the colored areas in the downslope side will be used to determine the volume of exchange flow in the study. Table 1 lists the experimental conditions and relevant parameters. $Re_{lower} \left(= \frac{\bar{u}_{lower} H_L}{\nu} \right)$, where \bar{u}_{lower} is the average lower toe current speed, H_L is the depth at the lock and $Re_{cy_{lower}} \left(= \frac{\bar{u}_{lower} d}{\nu} \right)$ are the Reynolds number and cylinder Reynolds number based

upon the average lower toe current speed. The shallow regions were filled with heavy (saline) fluid, so the experiments can represent real field conditions, in which the water temperature is cooler in shallow regions compared to deep regions. As a result, a model canopy in a shallow or deep region can simulate convective water exchange in the following conditions: (1) for a model canopy distributed in the shallows, the experiments can mimic exchange flows during daytime; and (2) a model canopy distributed in deeper regions but with heavy fluid in the shallows allows modelling the nighttime exchange flows. Because the heat fluxes between daytime heating and nighttime cooling are usually considered equal, experimental results can be applied to the entire diurnal cycle whether vegetation is present on the shallow or deep side. The ranges in water depth, H , and g' under typical field conditions are approximately 10 to 100 cm and 0 to 1 cm/s², respectively, yielding $u_{toe} \sim \sqrt{g'H_{max}} \sim O(10\frac{cm}{s})$, where H_{max} is the maximum water depth [8]. The reduced gravity, g' , in this study varied between 2 to 15 cm/s², and the maximum water depth ranged between 6 to 20 cm. Therefore, the scale of the current velocity in the experiments covered the same range as in typical field conditions. In Section 2, the mathematical formulation showed that several parameters need to be non-dimensionalized by the drag coefficient, C_D . As a result, a constant C_D value needs to be assigned. Based on Equation (13) with the current speed measured in Ho and Lin [25], C_D is simply set to 1, 1.75, and 2.5 for ϕ being 2.1%, 4.2%, and 6.9%, respectively.

Table 1. Summary of the experimental conditions and relevant parameters.

Run	S_0	g' (cm/s ²)	H_{max} (cm)	Vegetation Side	ϕ	d (cm)	Re_{lower}	Re_{cy_lower}
1	0.075	2.1	5.6	No	0	No	314	N.A.
2	0.075	2.1	5.4	Both	0.021	0.5	246	46
3	0.075	2.1	5.6	Both	0.042	0.5	227	41
4	0.075	2.1	5.4	Both	0.069	0.5	188	35
5	0.075	2.1	5.5	Shallow	0.021	0.5	292	N.A.
6	0.075	2.1	5.3	Shallow	0.069	0.5	230	N.A.
7	0.075	2.1	5.4	Deep	0.021	0.5	278	52
8	0.075	2.1	5.5	Deep	0.069	0.5	276	50
9	0.075	4.1	5.6	No	0	No	474	N.A.
10	0.075	4.1	5.6	Both	0.021	0.5	427	76
11	0.075	4.1	5.6	Both	0.069	0.5	358	64
12	0.075	4.1	5.5	Shallow	0.021	0.5	445	81
13	0.075	4.1	5.6	Shallow	0.069	0.5	479	86
14	0.075	4.1	5.4	Deep	0.021	0.5	470	87
15	0.075	4.1	5.5	Deep	0.069	0.5	445	81
16	0.075	7.2	5.7	No	0	No	759	N.A.
17	0.075	7.2	5.5	Both	0.021	0.5	674	123
18	0.075	7.2	5.6	Both	0.042	0.5	652	117
19	0.075	7.2	5.6	Both	0.069	0.5	638	114
20	0.075	7.2	5.5	Shallow	0.021	0.5	688	125
21	0.075	7.2	5.6	Shallow	0.069	0.5	782	140
22	0.075	7.2	5.6	Deep	0.069	0.5	718	128
23	0.125	2.1	9.5	No	0	No	752	N.A.
24	0.125	2.1	9.5	Both	0.021	0.5	571	60
25	0.125	2.1	9.6	Both	0.069	0.5	518	54
26	0.125	2.1	9.5	Shallow	0.021	0.5	670	71
27	0.125	2.1	9.5	Shallow	0.069	0.5	727	77
28	0.125	2.1	9.5	Deep	0.021	0.5	653	69
29	0.125	2.1	9.7	Deep	0.069	0.5	748	77
30	0.125	4.1	9.5	No	0	No	1110	N.A.

Table 1. Cont.

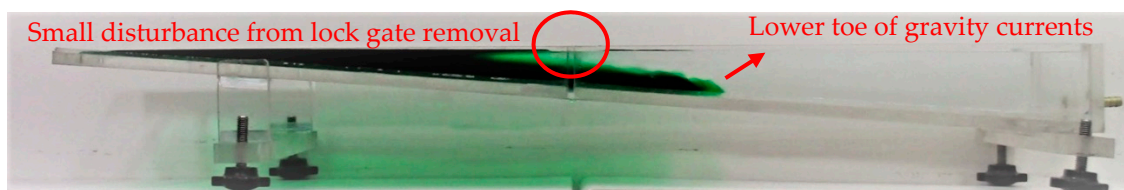
Run	S_0	$g'(\text{cm/s}^2)$	$H_{max}(\text{cm})$	Vegetation Side	ϕ	$d(\text{cm})$	Re_{lower}	Re_{cy_lower}
31	0.125	4.1	9.3	Both	0.021	0.5	1060	114
32	0.125	4.1	9.5	Both	0.069	0.5	1026	108
33	0.125	4.1	9.5	Shallow	0.069	0.5	1137	120
34	0.125	4.1	9.6	Deep	0.069	0.5	1099	114
35	0.125	7.2	9.6	No	0	No	1592	N.A.
36	0.125	7.2	9.5	Both	0.042	0.5	1382	146
37	0.125	7.2	9.7	Both	0.069	0.3	1328	82
38	0.125	7.2	9.5	Shallow	0.021	0.5	1435	151
39	0.125	7.2	9.5	Shallow	0.069	0.5	1637	172
40	0.125	7.2	9.5	Deep	0.069	0.5	1553	164
41	0.25	2.1	19.7	No	0	0	2602	N.A.
42	0.25	2.1	19.5	Both	0.069	0.3	2040	63
43	0.25	2.1	19.5	Shallow	0.069	0.3	2493	77
44	0.25	2.1	19.5	Shallow	0.069	0.5	2198	113
45	0.25	2.1	19.7	Deep	0.069	0.3	2107	64
46	0.25	4.1	19.5	No	0	0	3936	N.A.
47	0.25	4.1	19.5	Shallow	0.069	0.3	2942	91
48	0.25	4.1	19.5	Shallow	0.069	0.5	4019	206

Note: N.A. denotes “Not Applicable”.

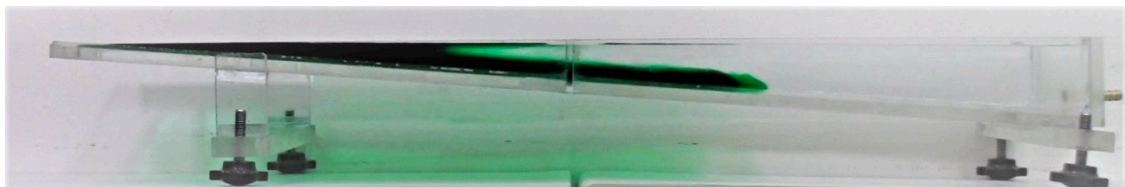
4. Results

4.1. Nature of Density-Driven Exchange Flows

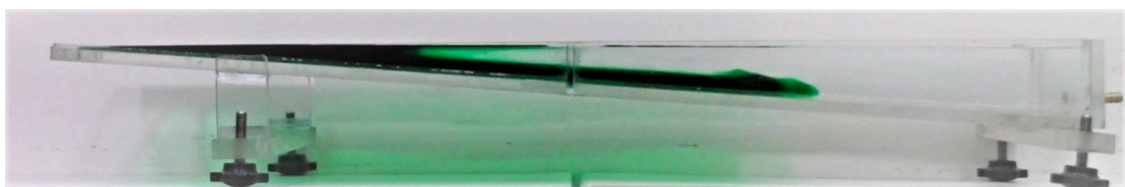
Gravity currents began to propagate downslope after the lock gate was swiftly removed, and the nature of the produced exchange flow (laminar or turbulent) is firstly determined. Very few studies have provided a specific value of the Reynolds number to determine if the density exchange flow laminar or turbulent. Ilıcak [33] used numerical simulations to show that the lock exchange flow is still laminar when the Reynolds number reaches 500. Hogg et al. [34] used a constant inflow device to observe the gravity current boundary and check when the flow becomes turbulent and perturbation at the interface of the current occurs. Their results showed that when the Reynolds number reaches 300, the disturbance at the interface of the current appears. For the experiments without a model canopy, we also used visual observations to determine whether the flow is laminar or turbulent and found that when the Reynolds number based upon the lower toe current speed Re_{lower} is larger than 340, some disturbance occurs at the back of current head (see Figure 3 below). In Figure 3a, the small disturbance shown (red circle) was due to the lock gate removal and disappeared rapidly. In Figure 3b,c, the interface of the current is smooth, and the flow can be regarded as laminar.



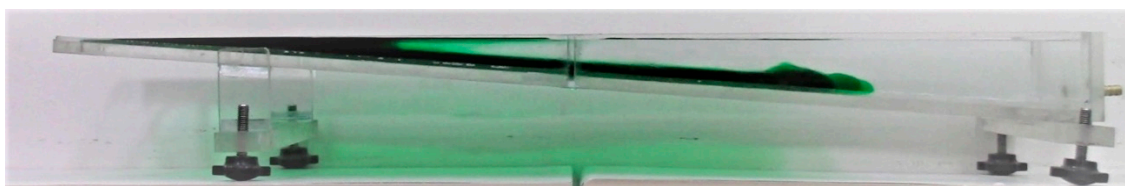
(a) $t = 11(\text{s}), u_{\text{lower}} = 0.89 \text{ cm/s}, Re_{\text{lower}} = 249$



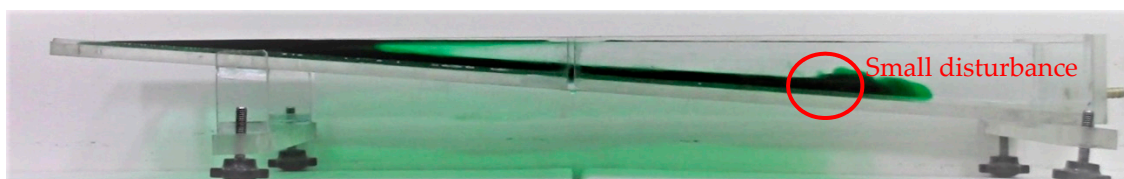
(b) $t = 15(\text{s}), u_{\text{lower}} = 1.02 \text{ cm/s}, Re_{\text{lower}} = 285$



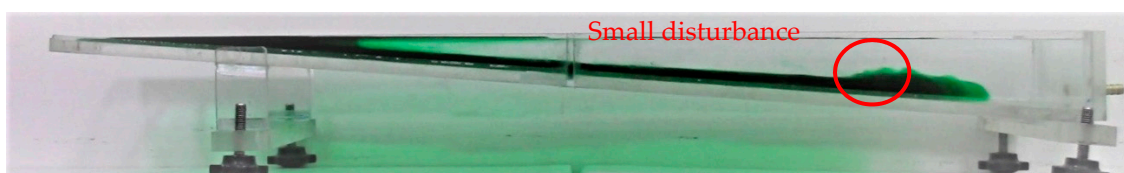
(c) $t = 19(\text{s}), u_{\text{lower}} = 1.10 \text{ cm/s}, Re_{\text{lower}} = 308$



(d) $t = 23(\text{s}), u_{\text{lower}} = 1.12 \text{ cm/s}, Re_{\text{lower}} = 313$



(e) $t = 27(\text{s}), u_{\text{lower}} = 1.22 \text{ cm/s}, Re_{\text{lower}} = 341$



(f) $t = 31(\text{s}), u_{\text{lower}} = 1.28 \text{ cm/s}, Re_{\text{lower}} = 358$

Figure 3. The time-series experimental images in Run 1 with the lower toe current speed u_{lower} and its corresponding Reynolds number, Re_{lower} .

As the current moves downslope further, the current speed and its Reynolds number Re_{lower} become larger. The disturbance at the interface of the current turns more obvious, i.e., the flow gradually becomes turbulent. Therefore, the Reynolds number Re_{lower} of approximately 340 could be

used as an indicator to determine if the gravity current is turbulent. In Table 1, the Reynolds numbers Re_{lower} for different runs are all larger than 340, implying that the experimental runs for the gravity current flowing downslope without a model canopy are all classified as turbulence in an average sense.

For the gravity currents within a model canopy, it is difficult to observe the interface of the current. Tanino and Nepf [35] used dye streaklines flowing within cylinder arrays to examine whether the flow is laminar or turbulent. They concluded that for the sparse (density $\phi = 0.01$) and dense ($\phi = 0.1$) canopy arrays, the flow patterns are laminar for their cylinder Reynolds number Re_{cy} less than 30, and turbulent eddies gradually appear at larger Re_{cy} . For the experimental runs for gravity currents within a model canopy, the corresponding Re_{cy} values are all larger than 30 (see Table 1), indicating that the nature of gravity currents for these runs are also turbulent.

4.2. Density-Driven Exchange Flow Patterns and Current Head Profiles

Figure 4 shows the pictures of gravity currents traveling down at two different vegetation configurations, i.e., a model canopy distributed in either a shallow or deep region. Although few wooden sticks were not perfectly vertical, the horizontal projected areas of the sticks were still identical as those of vertical ones, i.e., they would impose the same drag forces on the gravity current. The effects of flow velocity not normal to the cylinders on drag forces will be discussed and evaluated in Section 5 Discussion. In Figure 4a, when a model canopy is only in deep regions, the model canopy allows less fluid flowing into the deep regions; the dense fluid thus accumulates in front of the model canopy, leading to the increases in the current thickness at the lock ($x = 0$). For the case of a model canopy distributed in shallows and open water in deep regions, the classic semi-elliptic head, and intense mixing and entrainment between the current and ambient fluid obviously appear in the downslope current (Figure 4b). In the shallow region, the interfacial profiles between the saline and fresh water in shallow regions perform like an inclined straight line (Figure 4b).

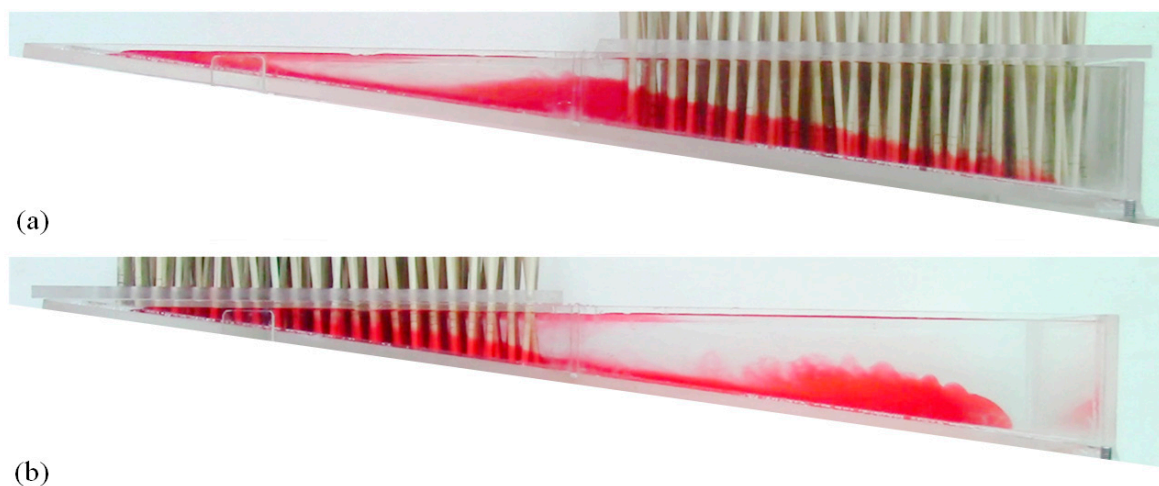


Figure 4. Images of gravity currents for two different configurations: (a) open water in shallows and a model canopy in deeper regions (Run 34); and (b) a model canopy in shallows and open water in deeper regions (Run 33).

To understand the combined effect of slope- and density-induced driving forces on downslope current motions, the interfacial profiles between the saline and fresh water are firstly investigated. Herein, the interfacial profiles in a milder slope with a smaller g' value or a moderate slope with a larger g' value on different vegetation configurations are exhibited. Figure 5 presents the temporal evolution of the interface between the saline and fresh water on a 4.3° slope at the same reduced gravity ($g' = 2.1 \text{ cm/s}^2$), but a model canopy ($\phi = 6.9\%$) occupies only a shallow or deep region while the other side is open water. When a model canopy is only in deep regions, the light fluid moving into

the shallows flows against the slope and thus decelerates with time. Thus, the interfacial profiles of the current in shallows resemble more of a parabolic shape than a semi-elliptical shape (Figure 5a). Furthermore, the model canopy in the deep region can reduce the downslope current and subsequently rise the current thickness at around the lock (Figure 5a). Within the model canopy, the interfacial profiles gradually form linear patterns as the current moves further into the model canopy. The classic semi-elliptical shape of the current head can only be found at the very front (Figure 5a). On the contrary, for the case of a model canopy distributed in shallows and open water in deep regions, the interfacial profiles in shallows perform like an inclined straight line. In deep regions, the classic semi-elliptical shape of the gravity current head is obvious when the current descends an unvegetated slope (Figure 5b), because gravity and buoyancy work in concert to accelerate the current. As the flow descends the slope, mixing and entrainment of the saline current with the ambient fluids gradually progress, while the current thickness at $x = 0$ remains nearly constant (Figure 5b).

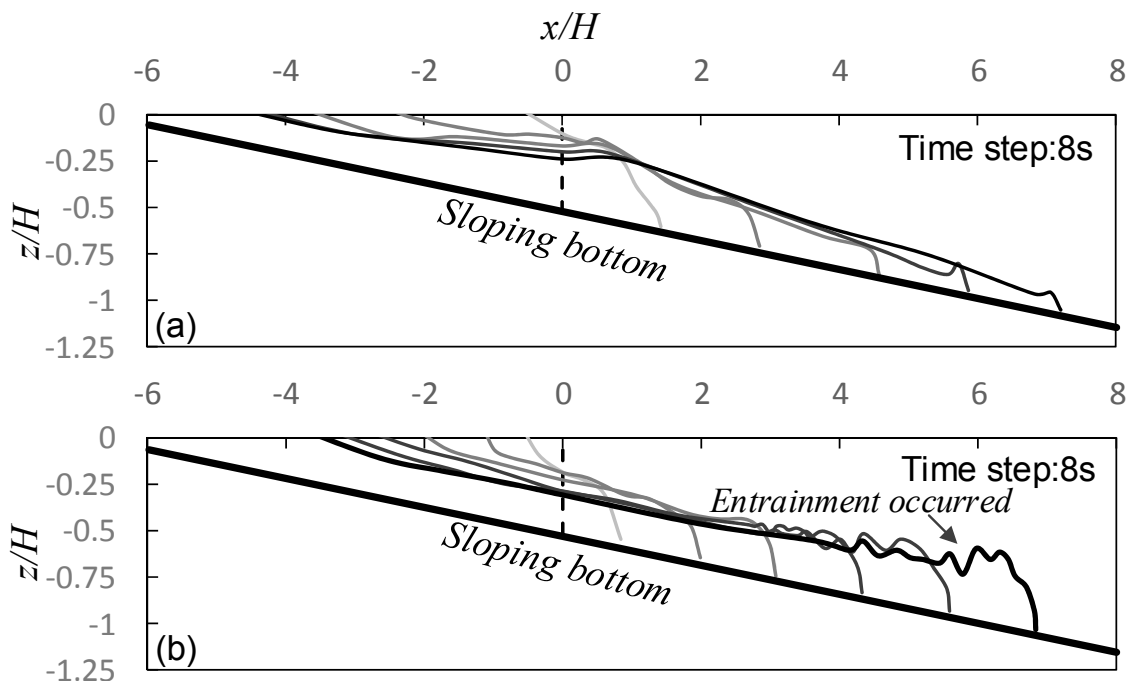


Figure 5. Temporal progression of the interface at a slope of 0.075 ($\sim 4.3^\circ$) and $g' = 2.1 \text{ cm/s}^2$: (a) Run 8 ($\phi = 0\%$ in shallows and $\phi = 6.9\%$ in deep regions); and (b) Run 6 ($\phi = 6.9\%$ in shallows and $\phi = 0\%$ in deep regions). The dashed line is the location of the lock, and the time interval between each profile is provided on the top of each figure.

The temporal evolutions of the upper and lower toe locations of the gravity current, i.e., x - t curves, are shown in Figure 6, where $\bar{H} (= \frac{1}{2}H)$ is the mean water depth, i.e., the depth at the lock ($x = 0$). After the removal of the gate, the current experiences an unsteady period (also called the initial effect) until the semi-elliptical head is formed [31]. The toe locations during this period cannot be distinctly identified, and thus the data collected during the initial period are excluded in Figures 6 and 7. Vertical error bars are added in Figures 6 and 7 to reflect the uncertainty in determining the propagation distance of gravity currents. Based upon the slope of x - t curves, the current velocity can be estimated. When the model canopy is in deep regions, the mean downslope current velocity (black line in Figure 6a) is faster than that when the model canopy is in shallows (grey line in Figure 6a). The results can be attributed to two reasons: (i) the conveyance areas inside the model canopy are reduced, and thus the current speed increases; (ii) the increased current thickness at the lock enlarges the pressure gradient between the current body and the current head, which leads to greater current head speeds.

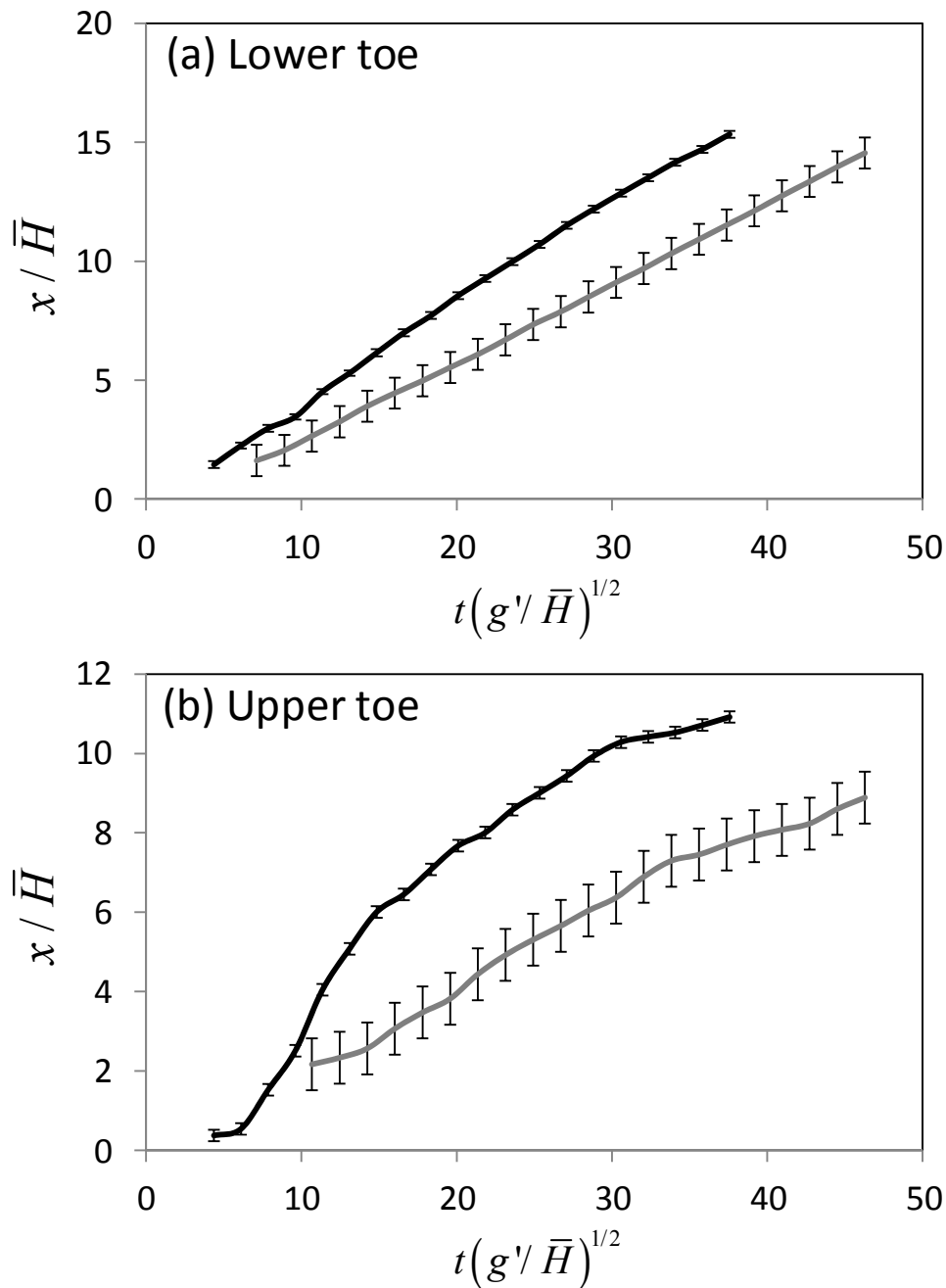


Figure 6. Temporal evolution of the lower and upper current toe positions at a slope of 0.075 ($\sim 4.3^\circ$) and $g' = 2.1 \text{ cm/s}^2$: (a) lower toe and (b) upper toe. Note: “—”: 6.9% model canopy distributed in deep regions (Run 8), and “—”: 6.9% model canopy distributed in shallows (Run 6).

For the upper toe, the mean current velocity within and without a model canopy exhibits two different trends. When a model canopy is absent in shallows, the slope of x - t curves, i.e., the current velocity, show a two-stage change (black line in Figure 6b): the mean current velocity is initially large and then gradually reduced. The initially greater current velocity is due to the inertia of the current, and the decreasing current velocity at the later stage is because viscosity increases as the current approaches the tip of the domain, i.e., a shallower water depth. For the presence of a model canopy in shallows, the mean current velocity in the upper toe is approximately constant during the whole course (grey line in Figure 6b). This result implies that the viscous effect is insignificant even in a

shallow water depth within vegetation, and the vegetation drag becomes dominant to determine the current velocity.

Figure 7 compares the cases in a relatively large reduced gravity ($g' = 7.2 \text{ cm/s}^2$), i.e., larger driving forces. In Figure 7a (lower current toe), when the dimensionless time is less than 10, the x - t curves for a model canopy in either shallow (grey line) and deep regions (black line) are overlapped. Until the dimensionless time is larger than 10, the model canopy in deep regions gradually decreases the current speed, and therefore the current speed, i.e., the slope of the x - t curves for a model canopy in deep regions (black line), is smaller than that for a model canopy in shallow regions (grey line). In Figure 7b (upper current toe), the initial gate removal affects the x - t curves for a model canopy in shallow or deep regions. However, the speeds of the upper current toe (the slope of the x - t curves) are similar, implying that the model canopy has almost no effect on current speed in shallow regions. In comparison with Figure 6, the x - t curves in Figure 7 for a canopy model in shallow and deep regions are relatively similar, suggesting that the location of a model canopy either in shallow or deep water plays a minor role rather than the reduced gravity, namely, the driving force of gravity current. In summary, the driving force (reduced gravity and tank slope), vegetation density and distribution could affect the lower and upper toe positions. If the driving force is larger, i.e., greater reduced gravity or larger tank slope, vegetation density and distribution will slightly affect the lower and upper toe positions. On the other hand, if the driving force is smaller, the vegetation density and distributions can result in significant differences in the lower and upper toe positions.

As the reduced gravity and tank slope become larger, the interfacial profiles of the gravity current exhibit different patterns (Figure 8). For a model canopy only distributed in deep regions, the saline fluid in the shallows rapidly descends but is arrested in front of the model canopy, causing the rising interface at the lock ($x = 0$) (Figure 8a). Once the current gradually flows into the model canopy, the original jammed saline fluid slowly drains along the slope, and the elevated interface at the lock decreases. In contrast, when there is a model canopy in the shallows, the thickness of the current at the lock rapidly decreases as the current moves into the open and deep regions (Figure 8b). With the thinning current thickness, the current head tends to detach (or separate) from the current body, as mentioned by Nogueira et al. [36] in the study of gravity current over a rough and flat bed. The thinning current body is because the major saline fluid is trapped within a model canopy in the shallow region, and sufficient fluid cannot be immediately supplied to the current head in the deep region. Without enough fluid supply, the current head moves as an individual body and accelerates along the downslope course. The thinning body between the leading and trailing parts of the density current causes a greater current head velocity but less exchange volumetric discharge in comparison to the case of a model canopy distributed in deep regions. This phenomenon can be observed more clearly in the temporal variations of the current thickness, h_d , at the lock (Figure 9).

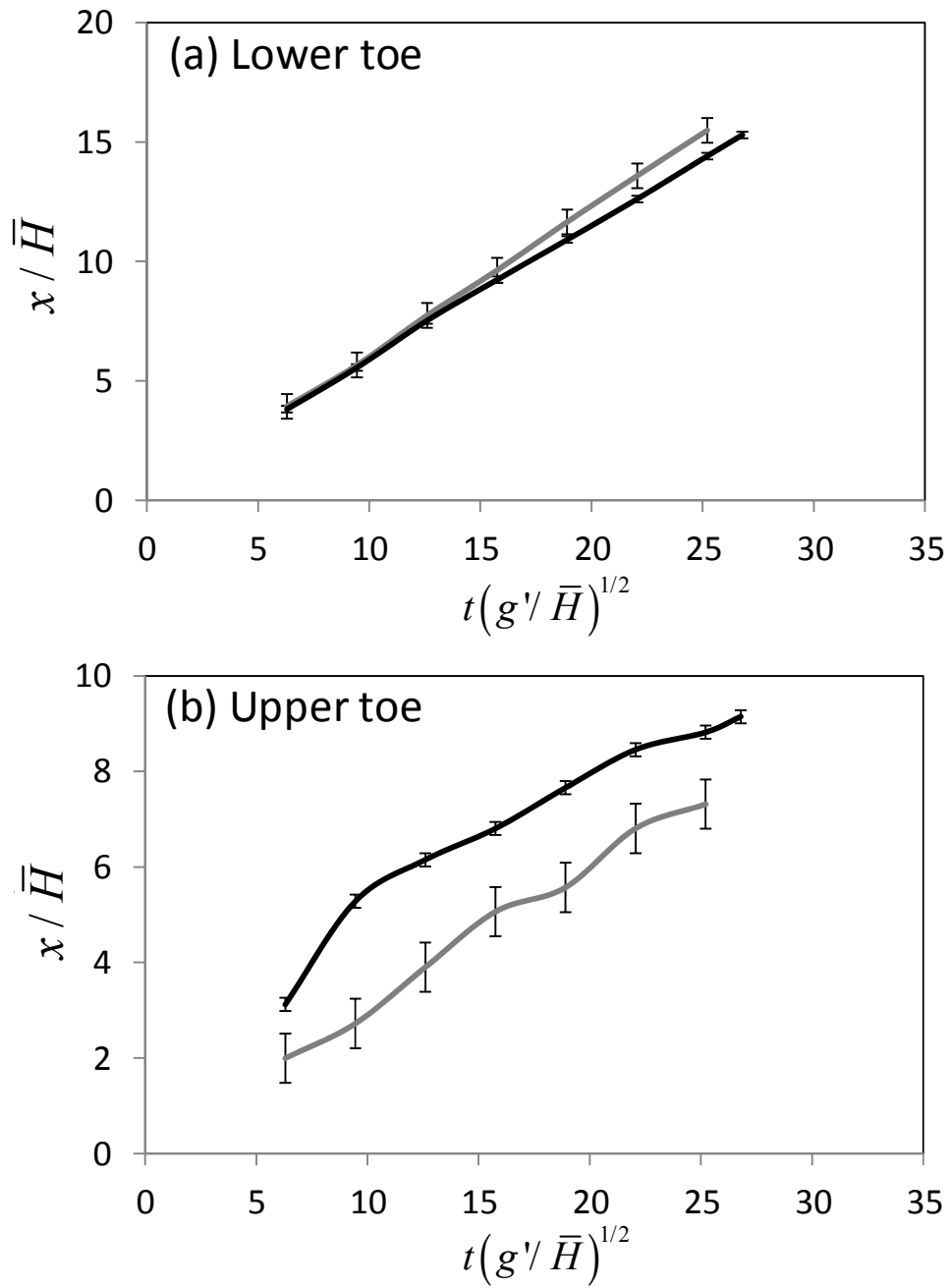


Figure 7. Temporal evolution of the lower and upper toe positions at a slope of 0.075 (~4.3°) and $g' = 7.2 \text{ cm/s}^2$: (a) lower toe and (b) upper toe. Note: “—”: 6.9% model canopy distributed in deep regions (Run 22), and “- - -”: 6.9% model canopy distributed in shallows (Run 21).

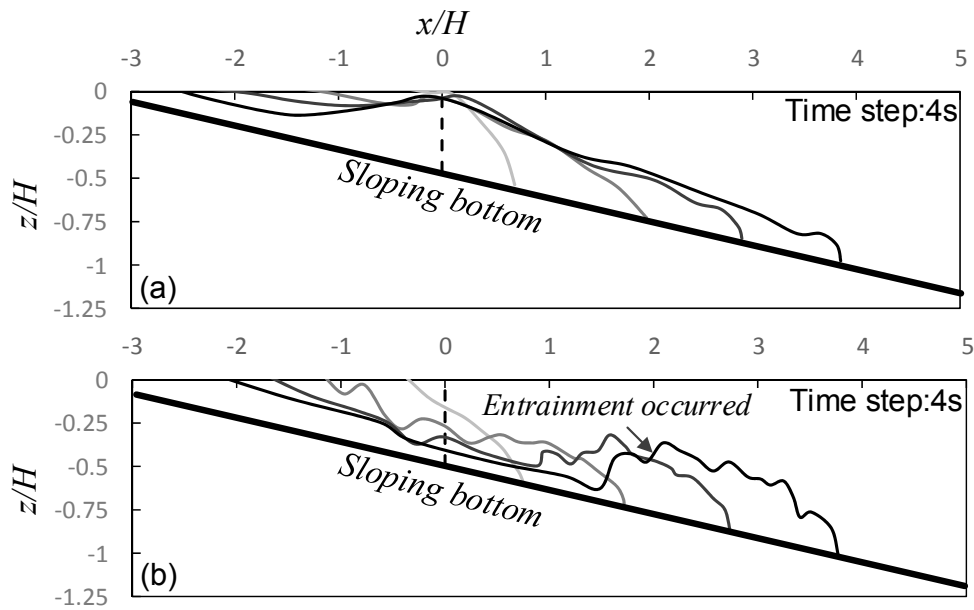


Figure 8. Temporal progression of the interface at a slope of 0.125 ($\sim 7.1^\circ$) and $gt = 7.2 \text{ cm/s}^2$: (a) Run 34 ($\phi = 0\%$ in shallows, and $\phi = 6.9\%$ in deep regions); and (b) Run 33 ($\phi = 6.9\%$ in shallows, and $\phi = 0\%$ in deep regions).

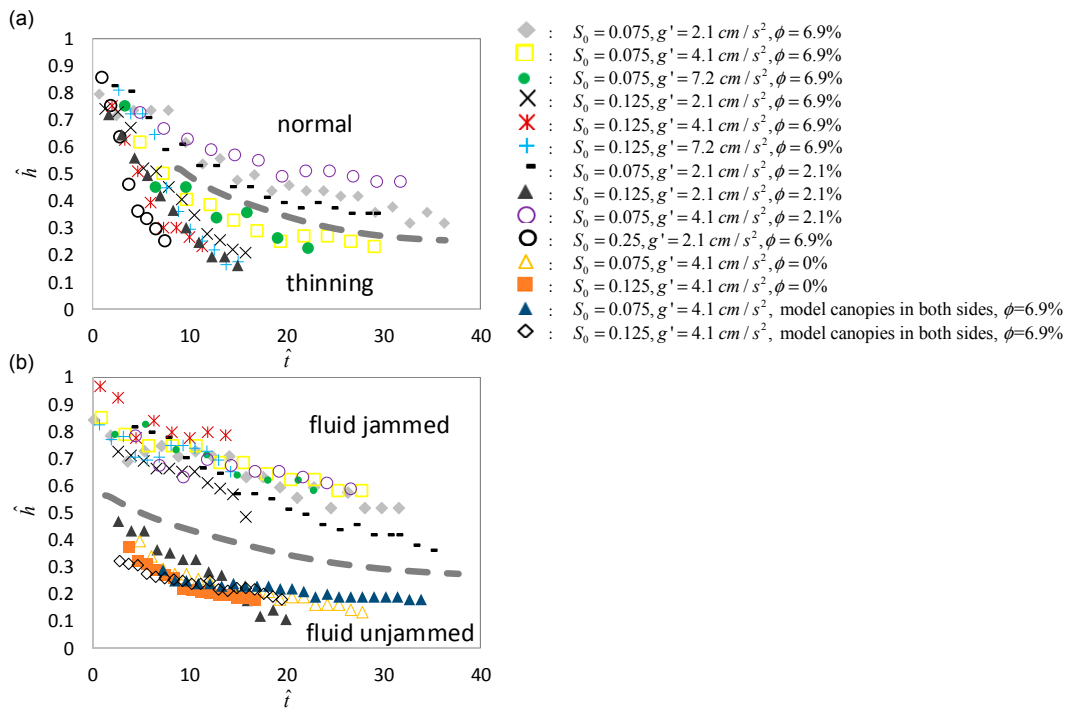


Figure 9. Normalized temporal variation in current thickness at the lock of the tank: (a) a model canopy distributed in shallows; and (b) a model canopy distributed in deep regions.

4.3. Current Thickness of Density-Driven Exchange Flows

The current thickness, h_d , is made dimensionless with the mean water depth \bar{H} , $\hat{h} = \frac{h_d}{\bar{H}}$ and the time, t , after the lock removal as $\hat{t} = t\sqrt{\frac{g'}{\bar{H}}}$. For a model canopy distributed in shallows and open water in deep regions, $\hat{h} - \hat{t}$ curves perform exponential decay at various rates (Figure 9a). This reflects

the consequences that the current tails are trapped within the model canopy and the lower current toe moves downslope at a faster speed; the current thickness becomes thinner, which confirms the tendency of the current head and body to separate. The experimental results regarding the current thickness at the lock can be manually categorized as the “thinning” or “normal” cases (see the dashed line in Figure 9a), where “thinning” means that the current thickness at the lock reduces rapidly and “normal” denotes the slow decrease of the current thickness. For the case of slope $S_0 = 0.075$ and $\phi = 6.9\%$ in the shallow region, when the reduced gravity g' is 2.1 cm/s^2 , the \hat{h} values at the lock do not significantly reduce. However, when the reduced gravity g' increases to 4.1 and 7.2 cm/s^2 , the lower current toe speed increases as well, and the \hat{h} curves at the lock transit from the “thinning” regime to the “normal” regime. When the bottom slope S_0 becomes 0.125 and $\phi = 6.9\%$ in the shallow region, even for the case of $g' = 2.1 \text{ cm/s}^2$, the \hat{h} curves would reach the “thinning” regime. Therefore, the “thinning” phenomenon is dependent on the speed differences of the current head and tail, which are determined by the tank slope, reduced gravity, and canopy density in shallows. However, it is difficult to determine the “thinning” criteria as the interaction between the aforementioned factors is complex and there are currently insufficient data.

When a model canopy is present in deep regions, \hat{h} versus \hat{t} data show two distinctly different groups: one group with higher \hat{h} values and the other with lower \hat{h} values (Figure 9b). Another dashed line drawn on Figure 9b can separate these two groups as “fluid jammed” and “fluid unjammed”. Both \hat{h} values from the two groups decrease at a similar pace as \hat{t} increases. The data with higher \hat{h} values (“fluid jammed” on Figure 9b) indicate that the saline fluid cannot swiftly flow through the model canopy, i.e., the saline fluid will jam in front of the model canopy. The occurrence of this fluid jam is due to the slower current head speed but faster current tail speed, i.e., the dense model canopy only in deep regions. In contrast, the data with smaller \hat{h} values (“fluid unjammed” on Figure 9b) suggest that the gravity current flows down the slope without difficulty. The “fluid unjammed” cases are mainly from the sparse model canopy only in deep regions. In Figure 9b, the cases conducted under conditions without a model canopy or with uniformly and fully distributed model canopies are also compared. For the cases without a model canopy or with uniformly and fully distributed model canopies, the $\hat{h} - \hat{t}$ data perform “fluid unjammed” patterns. For a sparse model canopy ($\phi = 2.1\%$) in deep regions, the downslope current speeds are the key to determine if the “fluid unjammed” pattern occurs. For a milder slope ($S_0 = 0.075$, see symbol ‘-’ in Figure 9b) with $\phi = 2.1\%$, i.e., slow downslope current speed, the “fluid jammed” pattern occurs, whereas for a steeper slope ($S_0 = 0.125$, see symbol ‘▲’ in Figure 9b) with $\phi = 2.1\%$, i.e., fast downslope current speed, the “fluid unjammed” pattern can be found. Therefore, it can be concluded that fluid-jamming phenomena only occurs when vegetation is present in deep regions, and the tank slope, reduced gravity and vegetation density in deep regions are key factors resulting in significant differences between current head and current tail speeds as well as subsequent fluid jamming. However, the transition from the “fluid unjammed” regime to the “jammed” regime is still unclear. Figure 9b does not show the transition cases from the “fluid unjammed” regime to the “jammed” regime. To understand its transition criteria, more laboratory experiments for different slopes and densities of a model canopy needs to be carried out in the future.

5. Discussions

5.1. Froude Numbers of Density-Driven Exchange Flows

The experimental results in four model canopy configurations including no model canopy, model canopies on both sides, and a model canopy in shallow or deep sides of tanks are firstly compared to discuss the effects of vegetation distribution on gravity current. Figure 10 presents the mean Froude number $Fr \left(= \frac{u_{toe}}{\sqrt{g'H}} \right)$ for four experimental configurations. The mean current speeds of the lower and upper toes are used to calculate the Fr values. For a gravity current over a smooth and flat bed, the Fr value is approximately equal to the value of 0.42 obtained from laboratory experiments [37]. When gravity current travels downslope in the absence of a model canopy, the Fr value based on the

lower toe speed is greater than for a flat bottom because of the slope-induced gravitational component. In general, this effect increases as the reduced gravity and the tank slope become larger. As the current flows to the tip of the tank, the current velocity of the upper toe is reduced owing to the downslope current motions and the viscous effect in shallow regions. When the reduced gravity g' is less than 7.2 cm/s^2 , the Fr value of the upper toe is smaller than that in flat bottom cases. At $S_0 = 0.075$, the Fr values of the lower and upper toes without a model canopy are generally larger than in the other three cases, indicating a faster mean current velocity in the lower and upper toes (Figure 10a,b). When model canopies occupy both sides of the tank, the Fr value is the smallest among the four canopy configuration, but there are several exceptions found here. For instance, when a model canopy only occupies the shallow regions, the lower toe speed grows faster as the reduced gravity g' increases than in the case with no model canopy (Figure 10a). This is possibly due to the thinning phenomenon between the lower and upper bodies of the current, which reduces the volume of the downslope current and causes faster lower toe speed. The upper toe velocities at $S_0 = 0.075$ for a model canopy distributed in deep regions are comparable or even faster than the case of no model canopy on either side (Figure 10b). The smaller conveyance areas within a model canopy and larger pressure gradient between the current body and head, as mentioned in the previous section, are possibly responsible for the result.

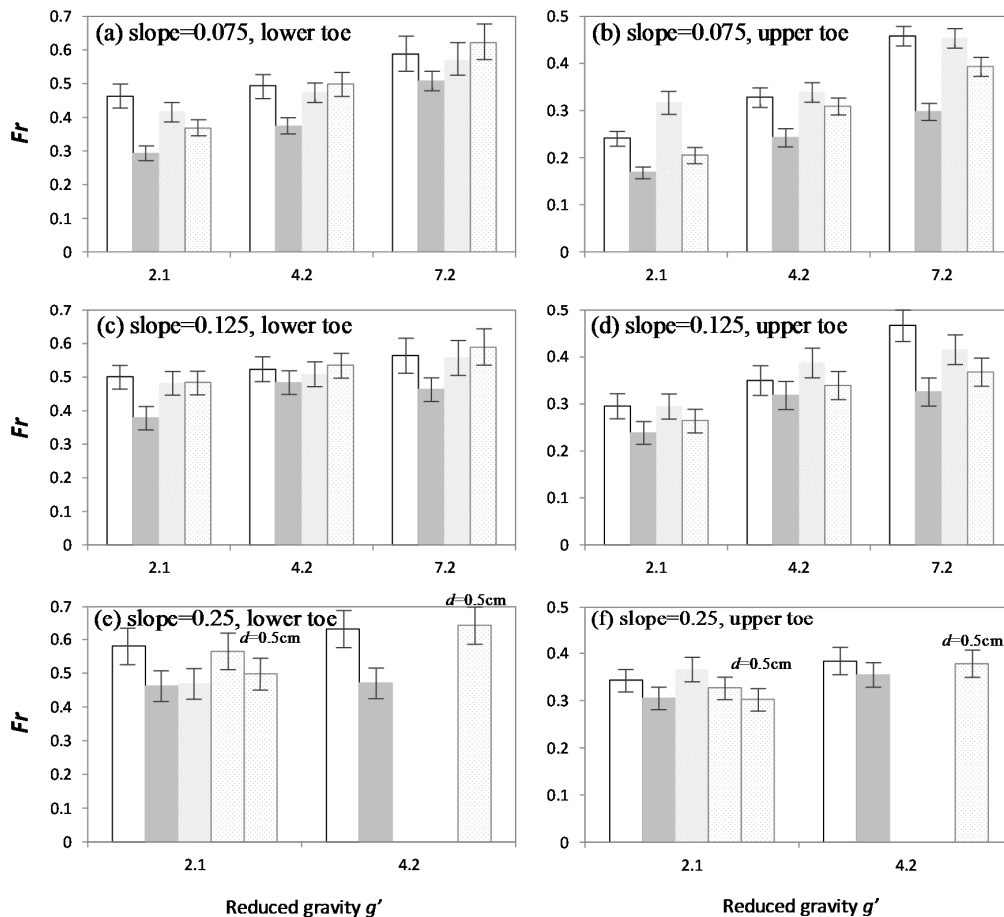


Figure 10. Mean Froude number ($Fr = \frac{u_{toe}}{\sqrt{g'H}}$) versus reduced gravity for $\phi = 6.9\%$. The symbols are as follows: ‘□’ = no model canopy; ‘■’ = model canopies on both sides; ‘▨’ = a model canopy distributed in deep regions; and ‘▩’ = a model canopy distributed in shallows. In (a–d), the canopy diameter is 0.5 cm, whereas canopy diameter is 0.3 cm in (e,f) except for the runs marked with “ $d = 0.5 \text{ cm}$ ”. Vertical error bars are determined from measurement errors.

At $S_0 = 0.125$ (Figure 10c,d), the Fr values among the four canopy configurations are closer to each other in comparison to the cases at $S_0 = 0.075$ (Figure 10a,b), indicating that the vegetation configurations have a larger impact for currents over small slopes ($S_0 = 0.075$) rather than over larger slopes ($S_0 = 0.125$). The lower toe velocities when a model canopy is only present in shallow regions gradually become larger as the reduced gravity increases, again confirming the thinning effect in the current body. When a model canopy is only in deep regions, the upper toe velocities at $S_0 = 0.125$ are also faster than the case without any model canopy until the reduced gravity reaches 7.2 cm/s^2 (Figure 10d). At the steep slope ($S_0 = 0.25$) and with 6.9% vegetation cover on both sides, the lower and upper toe current velocities and Fr values (≈ 0.45) are still larger than the flat bottom cases without a model canopy (Figure 10e,f). The experimental results on a 0.25 slope also reveal that a model canopy with a larger diameter can decrease current speed more than a smaller canopy diameter given the same canopy density and configuration.

5.2. Intrusion Length and Volume Discharge of Density-Driven Exchange Flows

Through the present experimental datasets, the relationships to quantitatively estimate the intrusion length and exchange flowrate through with different bottom slope and vegetation distribution are developed. The dimensionless intrusion length $\hat{L}_v \left(= \left(\frac{2}{3} \right)^{2/3} L_v \left(\frac{nH^2}{C_D a} \right)^{-1/3} \right)$ against \hat{t} when the model canopy is distributed in either the shallow or deep sides is presented in Figure 11 and compared with the regression curves obtained from Zhang and Nepf [20].

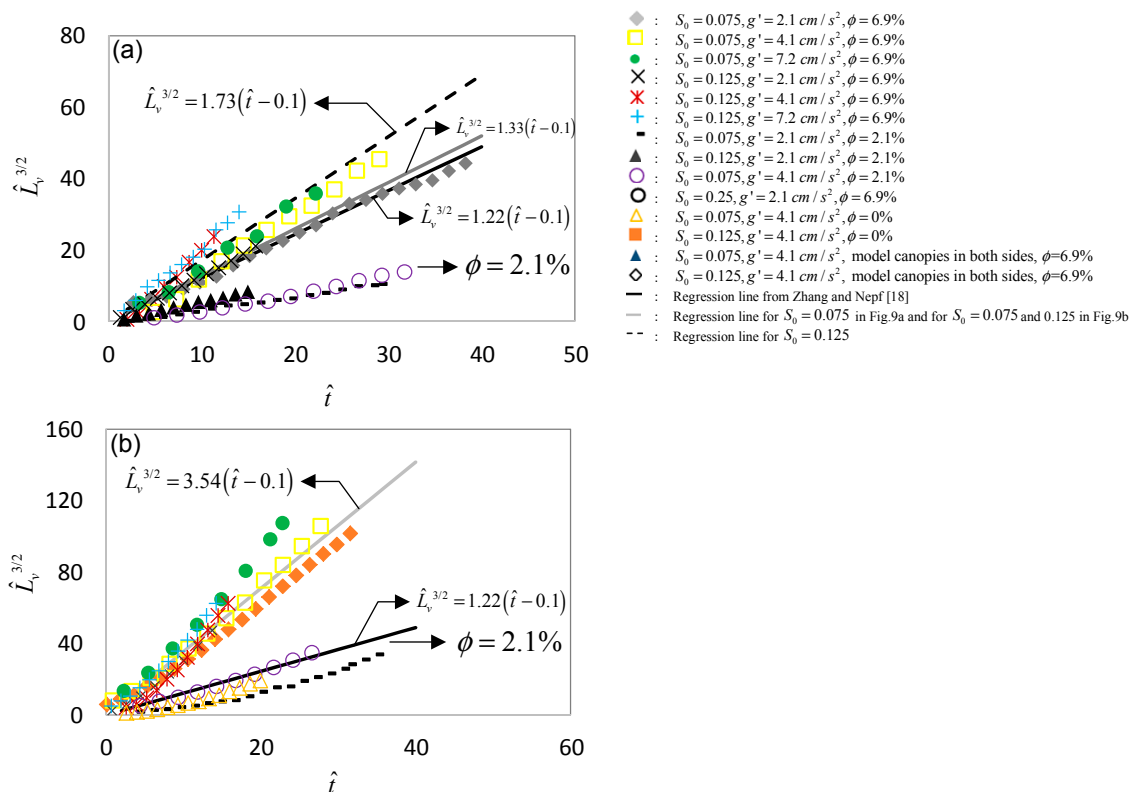


Figure 11. Normalized temporal variation in the intrusion length of the currents: (a) vegetation distributed in shallows; and (b) vegetation distributed in deep regions.

The results show that the \hat{L}_v value at $\phi = 2.1\%$ is much smaller than in the other cases where the vegetation density ϕ is 6.9% as well as the results from [20] (Figure 11a). This is because the derivation from Zhang and Nepf [19] assumes the dominance of vegetative drag on the flow motions; however, the flow condition within a sparse model canopy is inertially controlled. Hence, these data will be

excluded in the following regression analysis. Over a flat bed, the dimensional intrusion length \hat{L}_v versus \hat{t} can be expressed as [19]:

$$\hat{L}_v^{3/2} = 0.77(\hat{t} - \hat{t}_0) \quad (14)$$

where \hat{t}_0 is the dimensionless initial period of inertial flow and equals to 0.1. In this study, we assume that $\hat{L}_v(\hat{t}_0)$ as well as $\hat{V}_v(\hat{t}_0)$ follow the same formulaic forms, i.e., $\hat{L}_v^{3/2} \propto (\hat{t} - \hat{t}_0)$ and $\hat{V}_v \propto (\hat{t} - \hat{t}_0)^{0.74}$, in Zhang and Nepf [19], but the coefficient in front of $(\hat{t} - \hat{t}_0)$ must be fitted with the present experimental data. The advantage to making these assumptions is that the differences in intrusion length and exchange volume discharge over a flat bed and sloping bed can be easily indicated by comparing the coefficients in front of the $(\hat{t} - \hat{t}_0)$ term in Equation (14). Since the drag coefficient, C_D , used in this study is larger than that in Zhang and Nepf [19] and \hat{L}_v is proportional to $C_D^{1/3}$, the \hat{L}_v versus \hat{t} profiles suggested by Zhang and Nepf [19] need to be accordingly adjusted, which is given by:

$$\hat{L}_v^{3/2} = 1.22(\hat{t} - \hat{t}_0). \quad (15)$$

For a model canopy in shallows, two regression lines with uncertainty for $S_0 = 0.075$ and 0.125 can be obtained:

$$S_0 = 0.075, \hat{L}_v^{3/2} = (1.33 \pm 0.16)(\hat{t} - \hat{t}_0), \quad (16)$$

$$S_0 = 0.125, \hat{L}_v^{3/2} = (1.73 \pm 0.36)(\hat{t} - \hat{t}_0). \quad (17)$$

It is confirmed that \hat{L}_v is a function of tank slope, S_0 , and that \hat{t} follows from the scaling analysis proposed in Section 2.

For a model canopy distributed in deep regions, data collected for $S_0 = 0.075$ and 0.125 approximately collapse all the cases, indicating that the scaling is universal (Figure 11b), i.e.:

$$\hat{L}_v^{3/2} = (3.54 \pm 0.59)(\hat{t} - \hat{t}_0). \quad (18)$$

The regression lines can represent the trend of the experimental data well, which justifies the validity of adopting the same formulaic form proposed by Zhang and Nepf [19].

Based upon the areas displaced by the saline fluid in the deep side of the tank and assuming the density current is two-dimensional flow, the total exchange volume per unit width, V , as well as exchange volumetric flowrate per unit width, q , can be estimated. For a 0.25 slope, the intense mixing at the interface between the water and saline fluid makes it difficult to estimate the exchange volume discharge and flowrate accurately, and therefore this analysis herein only focuses on the runs at the milder slopes ($S_0 = 0.075$ and 0.125). Figure 12 shows the temporal variation in the dimensionless total

exchange volume discharge per unit width $\hat{V} \left(= \frac{V}{\frac{1}{2} \left[\frac{3}{2} (n\bar{H}^2 s / C_D a)^{1/2} \right]^{2/3}} \right)$ at runs with a canopy density

$\phi = 6.9\%$, where s ($= 0.6$) is a scale constant, as proposed by Tanino et al. [8]. The results indicate that the $\hat{V} - \hat{t}$ data change with the tank slope for either a model canopy distributed in shallow or deep regions, and the induced discharges on a steeply sloping bed are larger than those over a mildly sloping bed. These results can also be found in Figure 8, in which the areas occupied by the saline fluid are larger for a model canopy distributed in deep regions than a model canopy distributed in shallows at any time instant. Furthermore, the total volume discharge also increases with increasing tank slope, and the $\hat{V} - \hat{t}$ data at the same bed slope approximately collapse together; i.e., a universal equation can be obtained for an individual slope. In this study, the formulaic form derived in Zhang and Nepf [19], i.e., $\hat{V} = a(\hat{t} - \hat{t}_0)^{0.74}$, where a is fitted with experimental data, is adopted to represent the $\hat{V} - \hat{t}$ curves.

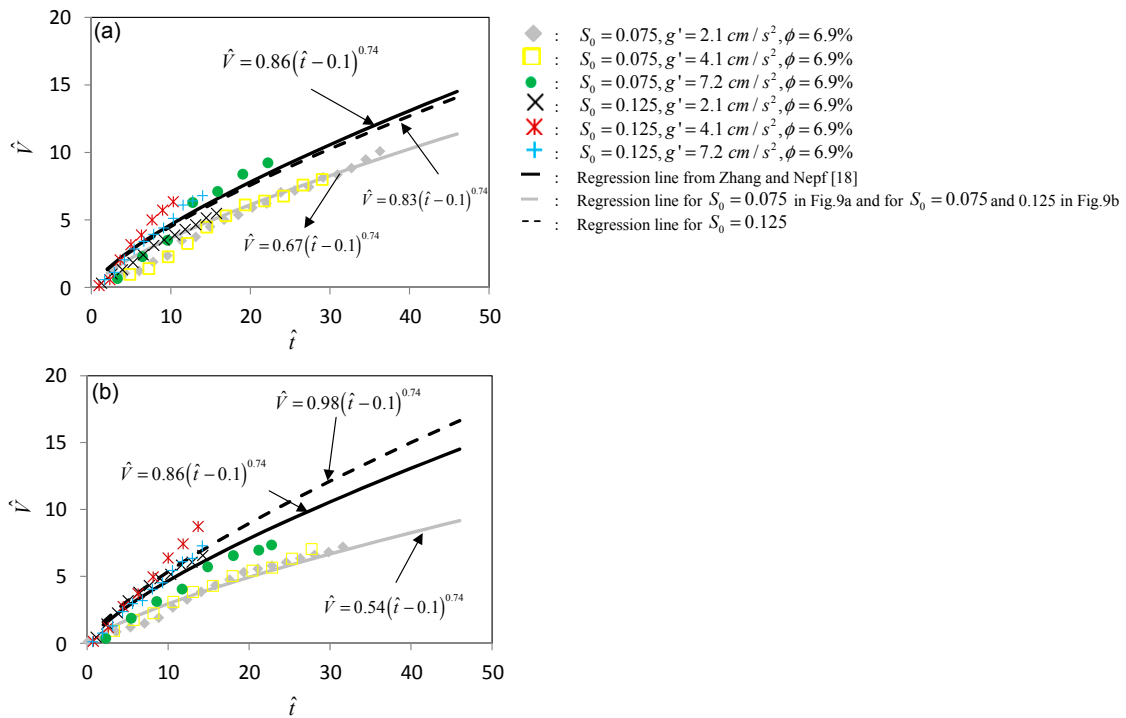


Figure 12. Temporal variation in the total volume discharge per unit width: (a) vegetation distributed in shallows and (b) vegetation distributed in deep regions.

The regressed $\hat{V} - \hat{t}$ curves with uncertainty are given as follows:

(a) A model canopy in shallows:

$$S_0 = 0.075, \hat{V} = (0.67 \pm 0.26)(\hat{t} - 0.1)^{0.74 \pm 0.30}, \tag{19}$$

$$S_0 = 0.125, \hat{V} = (0.83 \pm 0.24)(\hat{t} - 0.1)^{0.74 \pm 0.22}. \tag{20}$$

(b) A model canopy in deep regions:

$$S_0 = 0.075, \hat{V} = (0.54 \pm 0.18)(\hat{t} - 0.1)^{0.74 \pm 0.24}, \tag{21}$$

$$S_0 = 0.125, \hat{V} = (0.98 \pm 0.23)(\hat{t} - 0.1)^{0.74 \pm 0.18}. \tag{22}$$

The original $\hat{V} - \hat{t}$ curve in Zhang and Nepf [19] is: $\hat{V} = (0.63 \pm 0.18)(\hat{t} - 0.1)^{0.74 \pm 0.08}$, but since \hat{V} is proportional to $C_D^{1/3}$, the $\hat{V} - \hat{t}$ curve in Zhang and Nepf [19] is revised to $\hat{V} = (0.86 \pm 0.25)(\hat{t} - 0.1)^{0.74 \pm 0.08}$ (black line on Figure 12).

Figure 13 provides the normalized volumetric discharge rate, $\hat{q} \left(= \frac{q}{\sqrt{g'H^3}} \right)$, versus the dimensionless vegetation drag, $\left(= \frac{C_D a \bar{H}}{n} \right)$, within uniformly and fully distributed model canopies. It seems that the discharge rate \hat{q} value exhibits an exponential decay as $\frac{C_D a \bar{H}}{n}$ increases and strongly depends on the tank slope; i.e., a large slope can induce more exchange flows given the same $\frac{C_D a \bar{H}}{n}$.

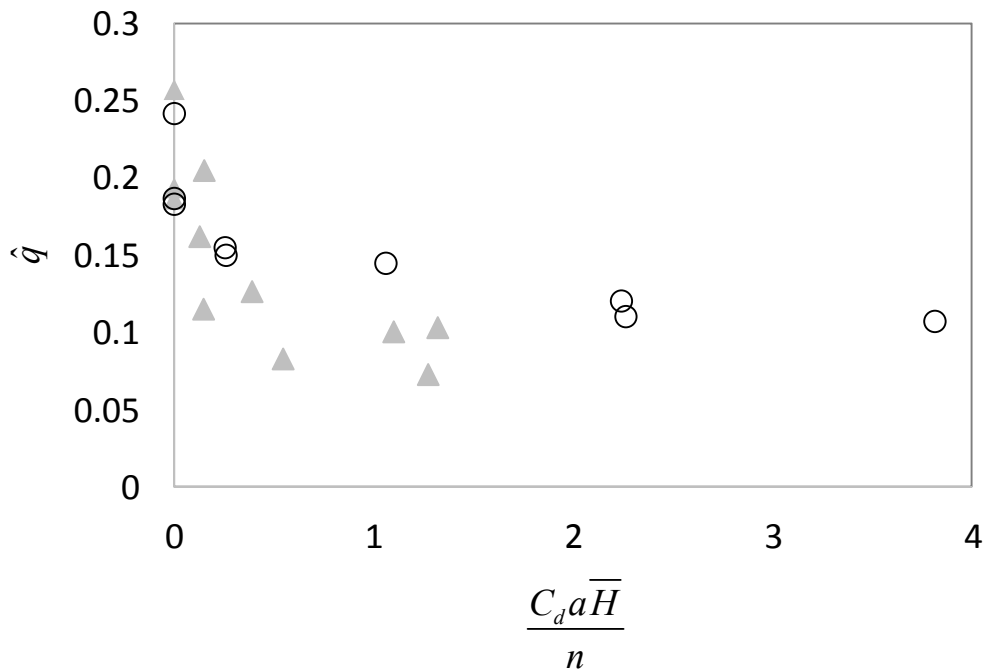


Figure 13. The variation in the normalized discharge rate $\hat{q} \left(= \frac{q}{\sqrt{g'H^3}} \right)$ versus $\frac{C_D a \bar{H}}{n}$ for the runs within a uniformly distributed canopy. Note: '▲' represents the cases on a 0.075 (~4.29°) slope, and '○' represents the cases on a 0.125 (~7.13°) slope.

Figure 14 shows $\hat{q} \left(= \frac{q}{\sqrt{g'H^3}} \right)$ versus $\frac{C_D a \bar{H}}{n}$ when a model canopy only occupies one side of the tank. Although the data points are scattered, some trends still can be found. \hat{q} possibly exhibits two different trends with the increase in $\frac{C_D a \bar{H}}{n}$ (Figure 14); one decreases linearly, and the other decays exponentially. The data showing a linear decrease are mainly from the cases on a steep slope ($S_0 = 0.125$) or on a mild slope with a larger gravitational acceleration ($g' \geq 4.1 \text{ cm/s}^2$), leading to larger downslope current speeds. In contrast, the data following an exponential decay are obtained from runs on milder slopes or steeper slopes with a smaller g' , resulting in slower downslope current speeds. For runs with a linear decrease, their Fr values range from 0.48 to 0.62, whereas for runs with exponential decay, the Fr values vary from 0.37 to 0.50. Therefore, the $Fr (\approx 0.50)$ value could possibly be an indicator to distinguish the two regimes for the discharge rate \hat{q} . The data in Figure 14 are scattered and can lead to more uncertainty when one generates a regression curve. Instead, the $\hat{V} - \hat{f}$ data shown in Figure 12 can obtain a more reliable regression curve to estimate the total exchange volumetric discharge.

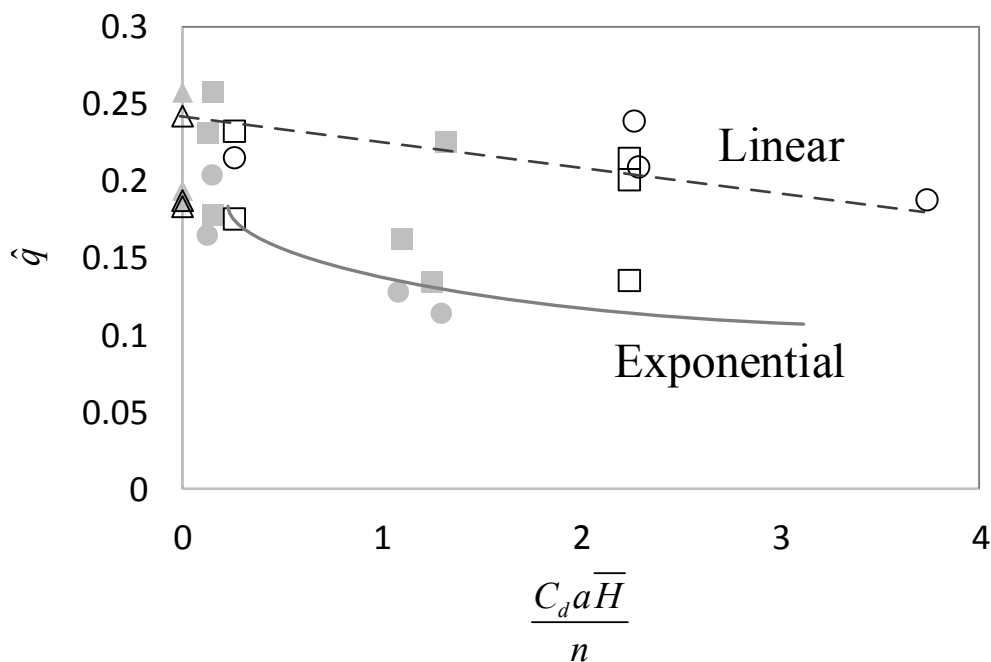


Figure 14. The variation in the normalized discharge rate \hat{q} ($= \frac{q}{\sqrt{g'H^3}}$) versus $\frac{C_d a \bar{H}}{n}$ for the runs in which a model canopy only occupies half of the domain. Note: '△' and '△' represent the runs without a model canopy on 0.075 (~4.29°) and 0.125 (~7.13°) slopes, respectively; '●' and '○' denote the runs with a model canopy distributed in deep regions on 0.075 (~4.29°) and 0.125 (~7.13°) slopes; and '■' and '□' indicate the runs with a model canopy distributed in shallows on 0.075 (~4.29°) and 0.125 (~7.13°) slopes. Dashed line shows the linearly decreasing trend, whereas gray solid line displays the exponentially decaying trend.

In the study of Zhang and Nepf [19], the developed formulas were used to estimate the intrusion length \hat{L}_v and the total exchange volume \hat{V} in a real field system (wetland). Since the formulaic forms adopted in this study are the same as those in Zhang and Nepf [19], the differences of the intrusion length and the total exchange volume among different vegetation distributions over a gentle or sloping bed can be estimated by simply comparing the coefficients in Equations (14)–(22). For example, if the vegetation is distributed in shallows the exchange flow can penetrate more deeply into the vegetation by ~6% and ~26% at slopes of 0.075 and 0.125, respectively, more than the flat bed cases in which the exchange flow can penetrate ~100 m into the vegetation. For vegetation distributed in deep regions, the intrusion length into the vegetation becomes double that of the case over a flat bed. These results imply that the exchange flow over a sloping bed can flush more areas than over a flat bed. Furthermore, the total exchange volume for vegetation distributed in shallow regions is decreased by ~22% and ~4% on slopes of 0.075 (mild) and 0.125 (steep), respectively, compared with that over a flat bed (the average discharge rate is $1.7 \text{ m}^3 \cdot \text{m}^{-1} \cdot \text{h}^{-1}$ in Zhang and Nepf [19]). In this calculation, the volume of heavy fluid over a flat bed is double that over a sloping bed, so the total exchange volume over a slope is smaller in some cases than over a flat bed. If the volume of heavy fluid is the same on flat and sloping beds, the total exchange volume over a slope would increase. For comparison, the total exchange volume in the case of vegetation distributed in deep regions is also estimated. The total exchange volume over a mild slope decreases by 37% while increasing by 14% over a steep slope compared with flat bed cases. The results presented above highlight the importance of bed slope and vegetation distribution in determining convective exchange flow.

5.3. Effects of Drag-Coefficient on Density-Driven Exchange Flows

Since the dimensionless intrusion length \hat{L}_v and volume \hat{V} both are proportional to $C_D^{-1/3}$, the coefficients and results obtained in Equations (14)–(22) can be significantly influenced by the vegetative drag coefficients C_D . For example, \hat{L}_v and \hat{V} estimated can be 60% larger for $C_D = 2.5$ in this study than for $C_D = 1$ in Zhang and Nepf [19]. The vegetative drag coefficient C_D which we adopted is based upon the best match of numerical results with the laboratory measurements [28]. It is still challenging to correctly estimate the C_D values within vegetation. In this study, the coefficients in Equations (14)–(22) were all gained from 6.9% dense vegetation cases. Thus, it is not possible to include the effects of vegetation density on coefficients in Equations (14)–(22). The comparisons obtained from Equations (14)–(22) assumed the same vegetation density but the vegetation configuration and nearshore slope were varied. It will be our future work to consider the effect of vegetation density in Equations (14)–(22).

For the sloping bottom, the current velocity is not normal to rigid cylinders, and the vortex shedding induced can be changed and subsequently affect the drag coefficient [38]. The “independence principle” is often used to consider the flow over inclined cylinders, where the flow velocity needs to be revised as normal to the cylinders [39]. According to the geometrical relation (see Figure 1), the lower toe current velocity component normal to the cylinders becomes $u_{lower} \cos \theta$. The independence principle works well for $\theta \leq 35^\circ$ [38] and can possibly extend to $\theta = 60^\circ$ [38].

By using the “independence principle”, the normal flow velocity is reduced by 3% for the steep slope cases ($S = 0.25$) and 0.3% for the mild slope cases ($S = 0.075$). Then, applying the cylinder Reynolds number-drag coefficient relation ($C_D \approx 1 + 50Re_{cy}^{-2/3}$), the current velocities u of 0.03 m/s and the diameter d of cylinders of 0.5 cm at $S = 0.25$, the drag coefficient C_D is reduced by 1%. Therefore, the effect of the current velocity not normal to rigid cylinders on drag resistance can be ignored for subsequent analysis.

6. Conclusions

Density-driven exchange flows, important to the transport of nutrients, pollutants and chemical substances in nearshore zones with weak wind conditions, were studied through laboratory lock-exchange experiments. Rigid and emergent cylinders were placed in one of two reservoirs, which were formed by partitioning a wedge-shaped laboratory tank, to represent aquatic canopies and simulate a partly vegetated slope. The most important finding from the experiments results was that a model canopy occupying only one side of the tank can result in variations in current head and tail speeds that subsequently create different flow patterns. For a model canopy in shallows and open water in deep regions, gravity currents trapped in shallows can result in less fluid into the current head, causing the body between the current head and current tail to thin due to a greater downslope current head speed. On the other hand, for a model canopy distributed in deeper regions with open water in shallows, gravity currents can potentially be jammed in front of the model canopy, which increases the thickness of the current at the center of the tank. Since the saline fluid can be regarded as a deformable and continuous body, the motion of the current on one side can somehow be influenced by that on the other side. By fitting with the experimental data, the equations for intrusion length and total exchange discharge can be obtained as they are functions of vegetation distribution, time and tank slope. The results also reveal that the total discharge rate generally decreases with increasing canopy drag. The key outcome of this study is to obtain the empirical equations that can be used to quantitatively estimate intrusion length and total volume exchange discharge in real field systems with different bottom slope and vegetation distribution. The evident differences on the estimates highlight the importance of bed slope and vegetation distribution in determining convective exchange flow. In order to meet real field conditions, future experiments will be carried out in tanks of various sizes, characterized by stratified environments. In addition, based upon the visual observations, the three-dimensional current behaviors may be important on measurement uncertainties, especially

for the cases without a model canopy. In this study, there is a lack of quantitative estimation on the effects. Future experiments need to address the issue as well.

Author Contributions: The methodology for the experiments was a joint effort of Z.G. and Y.-T.L. H.-C.H. and Z.W. were responsible for carrying out the experiments and analyzing the experiment data. Y.L. developed the theoretical model. Z.G. wrote the first draft of the paper, and H.-C.H., Z.W., and Y.-T.L. contributed to reviewing and editing the manuscript.

Funding: This research was funded by the National Key Research and Development Program of China (No. 2016YFC0401500), 3rd sub-topic (No. 2016YFC0401503), 7th sub-topic (No. 2016YFC0401507), and the National Natural Science Foundation of China (11672267).

Acknowledgments: The authors thank the editors and three anonymous reviewers for their constructive suggestions and comments for improvement of the paper.

Conflicts of Interest: The authors declare no conflict of interest.

References

- James, W.F.; Barko, J.W. Estimation of phosphorus exchange between littoral and pelagic zones during nighttime convection circulation. *Limnol. Oceanogr.* **1990**, *36*, 179–187. [[CrossRef](#)]
- MacIntyre, S.; Romero, J.R.; Kling, G.W. Spatial-temporal variability in surface layer deepening and lateral advection in an embayment of Lake Victoria, East Africa. *Limnol. Oceanogr.* **2002**, *47*, 657–671. [[CrossRef](#)]
- Woodward, B.L.; Marti, C.L.; Imberger, J.; Hipsey, M.R.; Oldham, C.E. Wind and buoyancy driven horizontal exchange in shallow embayments of a tropical reservoir: Lake Argyle, Western Australia. *Limnol. Oceanogr.* **2017**, *62*, 1636–1657. [[CrossRef](#)]
- Monismith, S.B.; Imberger, J.; Morison, M.L. Convective motion in the sidearm of a small reservoir. *Limnol. Oceanogr.* **1990**, *35*, 1676–1702. [[CrossRef](#)]
- Zhang, X.; Nepf, H.M. Thermally-driven exchange flow between open water and an aquatic canopy. *J. Fluid Mech.* **2009**, *632*, 227–243. [[CrossRef](#)]
- Coates, M.; Patterson, J.C. Unsteady natural convection in a cavity with non-uniform absorption of radiation. *J. Fluid Mech.* **1993**, *256*, 133–161. [[CrossRef](#)]
- Farrow, D.E.; Patterson, J.C. On the response of a reservoir sidearm to diurnal heating and cooling. *J. Fluid Mech.* **1993**, *246*, 143–161. [[CrossRef](#)]
- Tanino, Y.; Nepf, H.M.; Kulis, P.S. Gravity currents in aquatic canopies. *Water Resour. Res.* **2005**, *41*, W12402. [[CrossRef](#)]
- Adams, E.E.; Wells, S.A. Field measurements on side arms of Lake Anna, Va. *J. Hydraul. Eng.* **1984**, *110*, 773–793. [[CrossRef](#)]
- Sturman, J.J.; Ivey, G.N. Unsteady convective exchange flows in cavities. *J. Fluid Mech.* **1998**, *386*, 127–153. [[CrossRef](#)]
- Lei, C.; Patterson, J.C. Natural convection in a reservoir sidearm subject to solar radiation: Experimental observations. *Exp. Fluids* **2002**, *32*, 590–599. [[CrossRef](#)]
- Horsch, G.M.; Stefan, H.G. Convective circulation in littoral water due to surface cooling. *Limnol. Oceanogr.* **1988**, *33*, 1068–1083. [[CrossRef](#)]
- Lei, C.; Patterson, J.C. Natural convection induced by diurnal heating and cooling in a reservoir with slowly varying topography. *JSME Int. J. Ser. B Fluids Therm. Eng.* **2006**, *49*, 605–615. [[CrossRef](#)]
- Chimney, M.; Wenkert, L.; Pietro, K. Patterns of vertical stratification in a subtropical constructed wetland in south Florida (USA). *Ecol. Eng.* **2006**, *27*, 322–330. [[CrossRef](#)]
- Lövstedt, C.; Bengtsson, L. Density-driven current between reed belts and open water in a shallow lake. *Water Resour. Res.* **2008**, *44*, W10413. [[CrossRef](#)]
- Pokorný, J.; Kvet, J. Aquatic plants and lake ecosystem. In *the Lakes Handbook*; Blackwell Science Ltd.: Malden, MA, USA, 2004.
- Lightbody, A.F.; Awner, M.; Nepf, H.M. Observations of short-circuiting flow paths within a constructed treatment wetland in Augusta, Georgia, USA. *Limnol. Oceanogr.* **2007**, *53*, 1040–1053. [[CrossRef](#)]
- Coates, M.; Ferris, J. The radiatively driven natural and convection beneath a floating plant layer. *Limnol. Oceanogr.* **1994**, *39*, 1186–1194. [[CrossRef](#)]

19. Zhang, X.; Nepf, H.M. Density-driven exchange flow between open water and an aquatic canopy. *Water Resour. Res.* **2008**, *44*, W08417. [[CrossRef](#)]
20. Tsakiri, M.; Prinos, P.; Koftis, T. Numerical simulation of turbulent exchange flow in aquatic canopies. *J. Hydraul. Res.* **2016**, *54*, 131–144. [[CrossRef](#)]
21. Wietzel, R.G. Lake and river ecosystems. *Limnology* **2001**, *37*, 490–525.
22. Lin, Y.T.; Wu, C.H. The role of rooted emergent vegetation on periodically thermal-driven flow over a sloping bottom. *Environ. Fluid Mech.* **2014**, *14*, 1303–1334. [[CrossRef](#)]
23. Lin, Y.T.; Wu, C.H. Effects of a sharp change of emergent vegetation distributions on thermally driven flow over a slope. *Environ. Fluid Mech.* **2015**, *15*, 771–791. [[CrossRef](#)]
24. Ho, H.C.; Lin, Y.T. Gravity currents over a rigid and emergent vegetated slope. *Adv. Water Resour.* **2015**, *76*, 72–80. [[CrossRef](#)]
25. Benjamin, T.B. Gravity currents and related phenomena. *J. Fluid Mech.* **1968**, *31*, 209–248. [[CrossRef](#)]
26. Nepf, H.M. Drag, turbulence, and diffusion in flow through emergent vegetation. *Water Resour. Res.* **1999**, *35*, 479–489. [[CrossRef](#)]
27. Jamali, M.; Zhang, X.; Nepf, H.M. Exchange flow between a canopy and open water. *J. Fluid Mech.* **2008**, *611*, 237–254. [[CrossRef](#)]
28. Leonard, L.; Luther, M.E. Flow hydrodynamics in tidal marsh canopies. *Limnol. Oceanogr.* **1995**, *40*, 1474–1484. [[CrossRef](#)]
29. He, Z.; Zhao, L.; Lin, T.; Hu, P.; Lv, Y.; Ho, H.C.; Lin, Y.T. Hydrodynamics of gravity currents down a ramp in linearly stratified environments. *J. Hydraul. Eng.* **2017**, *143*, 04016085. [[CrossRef](#)]
30. Kadlec, R.H. Overland flow in wetlands: vegetation resistance. *J. Hydraul. Eng.* **1990**, *116*, 691–706. [[CrossRef](#)]
31. Wilson, R.I.; Friedrich, H.; Stevens, C. Turbulent entrainment in sediment-laden flows interacting with an obstacle. *Phys. Fluid* **2017**, *29*, 036603. [[CrossRef](#)]
32. Ilıcak, M. Energetics and mixing efficiency of lock-exchange flow. *Ocean Model.* **2014**, *83*, 179–187. [[CrossRef](#)]
33. Hogg, C.A.R.; Dalziel, S.B.; Huppert, H.E.; Imberger, J. Inclined gravity currents filling basins: The influence of Reynolds number on entrainment into gravity currents. *Phys. Fluid* **2015**, *27*, 096602. [[CrossRef](#)]
34. Tanino, Y.; Nepf, H.M. Lateral dispersion in random cylinder arrays at high Reynolds number. *J. Fluid Mech.* **2008**, *600*, 339–371. [[CrossRef](#)]
35. Nogueira, H.; Adduce, C.; Alves, E.; Franca, M. Analysis of lock-exchange gravity currents over smooth and rough beds. *J. Hydraul. Res.* **2013**, *51*, 417–431. [[CrossRef](#)]
36. Shin, J.O.; Dalziel, S.B.; Linden, P.F. Gravity currents produced by lock exchange. *J. Fluid Mech.* **2004**, *521*, 1–34. [[CrossRef](#)]
37. Vanatta, C. Experiments on vortex shedding from yawed circular cylinders. *AIAA J.* **1968**, *6*, 931–933. [[CrossRef](#)]
38. Shang, J.K.; Stone, H.A.; Smits, A.J. Flow past finite cylinders of constant curvature. *J. Fluid Mech.* **2018**, *837*, 896–915. [[CrossRef](#)]
39. Zhou, T.; Razali, S.M.; Zhou, Y.; Chua, L.; Cheng, L. Dependence of the wake on inclination of a stationary cylinder. *Exp. Fluid* **2009**, *46*, 1125–1138. [[CrossRef](#)]

